

The Centering of Optical Fiber Coatings by Monitoring Forward Scattering Patterns—Theory and Practice

By B. R. EICHENBAUM

(Manuscript received September 10, 1979)

The forward scattering pattern from a transversely illuminated polymer-coated optical fiber is modeled with a ray-tracing program. For polymers with a refractive index higher than that of silica, the scattering pattern contains caustic surfaces. If the coating is eccentric in a direction perpendicular to the incident rays, we show that the positions of the caustic surfaces (θ_A) vary monotonically with eccentricity at the rate of $0.85^\circ/\mu\text{m}$ for small eccentricities for a coating with a 1.539 refractive index and $59.3\text{-}\mu\text{m}$ thickness on a $110\text{-}\mu\text{m}$ diameter silica fiber. Another identifiable feature of the pattern (θ_B) has a predicted small-signal sensitivity of $1.1^\circ/\mu\text{m}$. The information obtained from the pattern can be used to insure well-centered coatings on optical fibers. A simple interpretation of the scattering pattern provides an error signal to guide compensatory coating cup alignment. The results are reported of well-centered runs obtained on two separate drawing lines by this means.

I. INTRODUCTION

The goal of placing an axially symmetric coating around an optical fiber has been experimentally approached through various techniques¹⁻⁴ and theoretically analyzed with various models.⁴⁻⁷ There is ample reason for this interest. Good centering has been shown to increase fiber strength.⁸ It also eases the fabrication of connector arrays for splicing and provides maximum abrasion protection for a given coating. Furthermore, an asymmetric coating may add to fiber loss.^{2,9}

For a coating that is fairly transparent and has a refractive index more than that of the fiber cladding, a light beam incident essentially transverse to the optic axis has been found to have a notably charac-

teristic forward scattering pattern. Its shape and position are easily monitored and provide unambiguous information about both coating thickness and eccentricity for any degree of eccentricity. The back-scatter pattern has been previously analyzed and used as an inline centering monitor.^{3,7}

In this paper, we describe the pattern, recount our experiences with it when used as a coating monitor, and present a ray trace model of the forward scattering. We use this model, together with a more limited closed form expression, to obtain a better understanding of the sensitivity and operating range of this monitoring technique. The pertinent parameters are coating refractive index, coating thickness, and eccentricity.

II. THEORY

Under appropriate values of coating refractive index, thickness, and eccentricity, an optical fiber illuminated as in Fig. 1 generates the scattering pattern shown in Figs. 2 and 3. We wish to predict the scattering angles θ_A and θ_B associated with the *A* and *B* boundaries

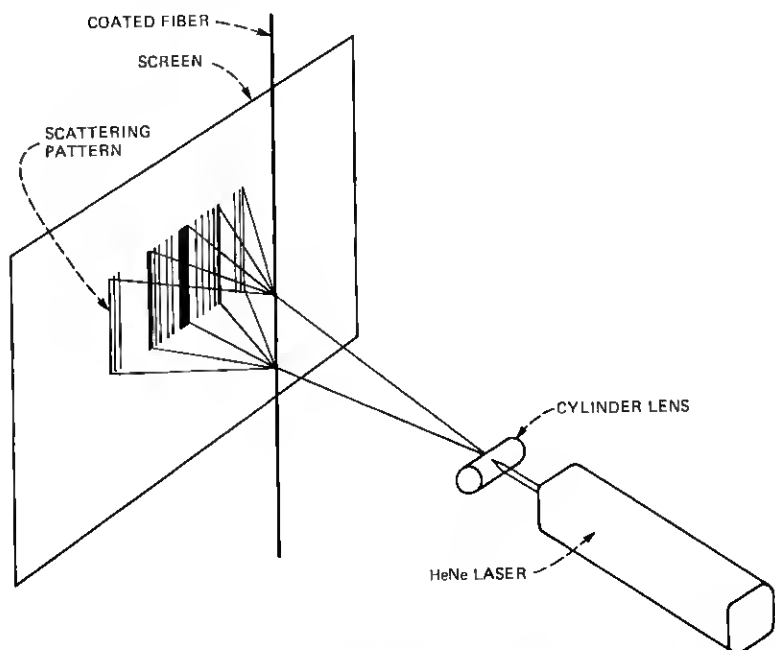


Fig. 1—Setup for generating the forward scattering pattern of a coated fiber off-line. A cylinder lens is used here to vertically expand the incident laser beam. This allows the coating geometry of a stationary fiber to be directly compared from point to point over the height of the pattern. Such vertical resolution may prove to be a useful tool for diagnosing coating defects (Ref. 3).

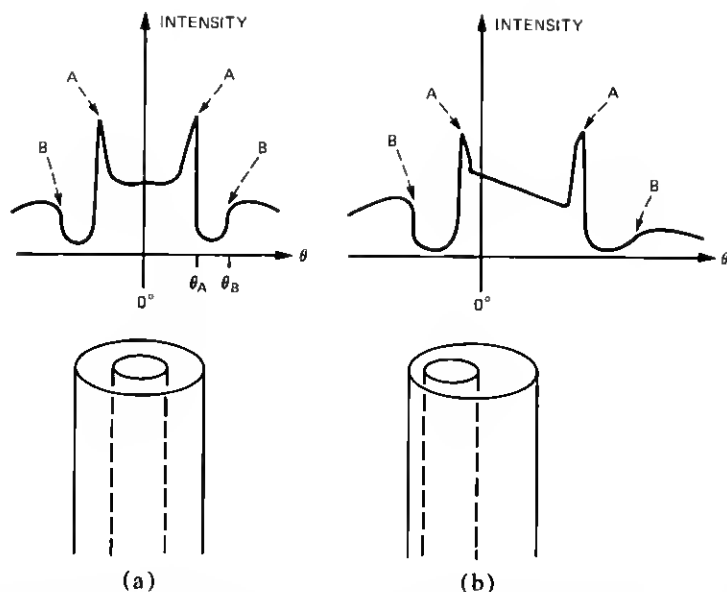


Fig. 2—Plot of the envelope of the characteristic scattering pattern intensities for (a) centered and (b) eccentric coatings (interference fringes ignored—see Fig. 3). There is a central bright zone between the points labeled A and another, but much less intense, bright zone beyond each B point.

between light and dark zones. Of special interest are the locations of the A boundaries. Their clear delineations enhance their potential as reference points for automated derivation of error signals.

Since our interest is primarily to predict the angles θ_A and θ_B , a prediction of the power envelope of the scattering pattern (as opposed to individual fringes) should suffice. This approach allows a variety of simplifications and the model thereby obtained can be characterized by the following list of assumptions:

1. Ignore phase and polarization of scattered radiation.
2. Assume both fiber and coating to be cylindrical, though not necessarily concentric.
3. Allow eccentricities only transverse to the incident rays.
4. Ignore Fresnel reflections.
5. Assume lossless dielectrics.
6. Assume $n = 1.457$ at 633 nm throughout cladding and core (ignore core profile).
7. Assume incident rays are all parallel and of uniform intensity.

As we shall see later, the model's predictions of θ_A and θ_B agree closely with the experiment. However, to appreciate its realm of applicability, some point-by-point justifying comments are helpful.

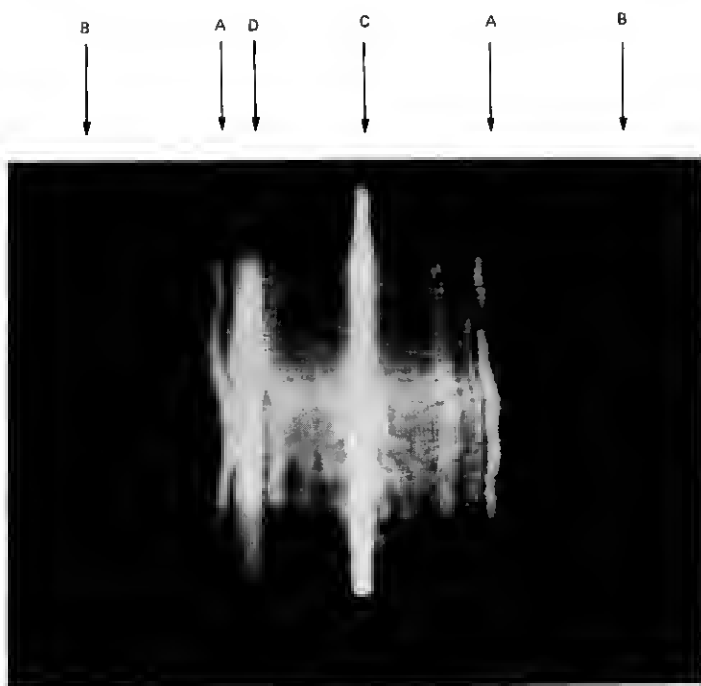


Fig. 3—Photograph of a scattering pattern from a cured, $n = 1.539$ coated fiber. Interference fringes can be seen (not included in Fig. 2). *A* and *B* indicate bright-dark boundaries as in Fig. 2. *C* marks that part of the incident beam that was not scattered by the fiber but continued straight on to the screen. *D* indicates an out-of-focus image of part of the fiber support and is unrelated to the pattern seen on the screen.

- (i) The inclusion of phase and polarization information in the scattered radiation would enable us to predict the structure of the interference fringes as was done by Watkins.¹⁰ But our current concern for merely the power envelope of the pattern led us to ignore these considerations. (If an automated scattering monitor is unavoidably affected by the interference pattern, then a refined, phase-sensitive model would be required for design guidance.)
- (ii) In the great majority of the coated fibers, both coating and fiber are nearly circular cylinders.
- (iii) While allowing only transverse eccentricity does restrict the applicability of the results, this is not troublesome from an instrumentation point of view. The inline monitoring equipment is always an orthogonal cross-beam set-up (see Section V), so that aligning for symmetry on one axis assures only transverse eccentricity on the other.
- (iv) Except for relatively few rays (near total internal reflection conditions), the Fresnel reflections carry too little power to

materially alter the high irradiance gradient observed at the boundaries, particularly the *A*-boundaries.

- (v) By reasoning similar to (iv), a small transmission loss through one pass of the coating can be ignored.
- (vi) Rays passing through the fiber core all lie within the bright central region of the scattering pattern and do not affect the contrast at *A* or *B*.
- (vii) The incident HeNe laser beam provides a reasonably plane and uniform intensity source over the <0.3-mm outside diameter of the coating.

The model is embodied in a ray-tracing Fortran computer program, VSCATE. Each ray is identified by its normalized height *H*, the height of the ray above the coating's center expressed as a fraction of the coating radius *r*₁ (see Fig. 4). After tracing the ray, we find it exits the coating at some angle, *θ*, relative to the incident direction. From the discrete pairs of values (*θ*, *H*), we can approximate *dθ(H)/dH*. The uniform incident radiation assumption then allows us to state

$$P(\theta) \propto \sum_H |d\theta(H)/dH|^{-1}, \quad (1)$$

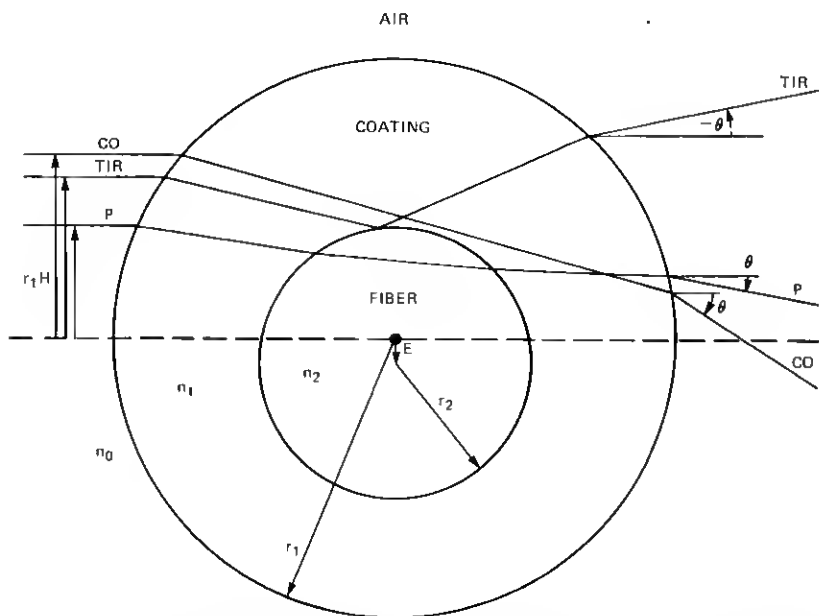


Fig. 4—The three characteristic types of ray paths: *P*—penetrates the fiber, *TIR*—undergoes a total internal reflection at the coating-fiber interface, and *CO*—passes through the coating only. Fiber radius is 55 μm , coating radius is 114.3 μm , and an eccentricity (*E*) of 10 μm exists. Refractive indices are $n_0 = 1.0003$, $n_1 = 1.539$, and $n_2 = 1.457$. Sign conventions for *E*, *H*, and scattering angles (*θ*) are indicated by the arrows. *H*-values are 0.40, 0.57, and 0.65 for the *P*, *TIR*, and *CO* rays, respectively.

where $P(\theta)$ is the power scattered per unit angle at θ . The summation is required because more than one H may correspond to a particular θ . For tracing rays incident below the coating's center ($H < 0$), we appeal to the symmetry

$$\theta(H, E) = -\theta(-H, -E), \quad (2)$$

where E is the signed eccentricity of the coating. The divergence of eq. (1) when $d\theta/dH = 0$ is a consequence of ignoring diffraction effects and is related to assumption 1 of the model. The integrated scattered power does not diverge, whether or not diffraction is included.

In Fig. 4, we have a cross section of a coated fiber with three rays traversing it, showing the sign conventions for H , E , and θ , and the three characteristic paths a ray may take once it enters the coating: (i) passes through the coating and penetrates (P) the fiber, (ii) experiences a total internal reflection (TIR) at the coating-fiber interface, and (iii) traverses the coating only (Co) and does not intercept the fiber. (Actually, a fourth possible path exists for sufficiently eccentric coatings in which a TIR occurs as the ray tries to exit the coating. This case is of significance only for large eccentricities as will be seen in Fig. 7.) The three rays illustrated were calculated by the VSCATE ray trace program with $n_0 = 1.0003$, $n_1 = 1.539$, and $n_2 = 1.457$, appropriate for a coating with a refractive index of 1.539 on a solid 100-percent silica fiber, surrounded by air.

Ray paths are uniquely determined by the H -value, refractive indices, and cross-section geometry. An equation representing each straight-line segment is obtained by appropriate application of either Snell's Law or a TIR at each preceding boundary. A simultaneous solution of this equation and the next boundary locus provides the next boundary intersection, whereupon the process repeats. Finally, as the ray exits the coating, its overall deviation θ from its original direction is related to the original H .

For the concentric coating case, $\theta(H)$ can be obtained in closed form by application of Bouguer's formula¹¹ without a ray trace. Details are given in Appendix A. A Fortran program, SCATCF, was written to evaluate the scattering pattern predicted by the closed form expressions. Although applicable only to the concentric case, it is valuable when compared to the more general ray trace approach as a check for mutual consistency between the models. Excellent agreement was found. For example, Figs. 8 and 9 can be obtained identically from either VSCATE or SCATCF. Also, the relatively simple form of SCATCF shows better the operating limits of the monitoring system in terms of coating thickness and refractive index. For example, if $n_2 r_2 / n_0 r_1 > 1$, then all arguments in eq. (11c) are less than unity for all values of H . We interpret such a condition to mean that eq. (11c) is valid for all

rays; that is, all rays penetrate the glass (*P*-rays). Similarly, if $n_2 r_2 / n_0 r_1 < 1$ and $n_1 r_2 / n_0 r_1 > 1$, then eq. (11b) is valid for some H ; that is, in addition to fiber-penetrating rays, some rays experience a TIR at the plastic-fiber interface (TIR-rays). But there are still no rays of the coating-only type (co-rays). Finally, if $n_1 r_2 / n_0 r_1 < 1$, then all types of rays are present and a full scattering pattern forms. Table I gives the conditions for the existence of the various rays and the values of H corresponding to each type.

III. PREDICTIONS

Plots of $\theta(H)$ are perhaps the clearest way to appreciate the origin of the light and dark zones. The solid line in Fig. 5 plots $\theta(H)$ for a fiber with a cured concentric $n = 1.539$ coating with $r_1 = 114.3 \mu\text{m}$ and $r_2 = 55.0 \mu\text{m}$. The assumed refractive index values are the same as those assumed in drawing the Fig. 4 rays. Upon comparing this result to the scattering of a homogeneous cylinder of $n = 1.539$ coating of $114.3\text{-}\mu\text{m}$ radius (long-dashed line), we note the following: (i) The two plots differ most dramatically at $H = n_2 r_2 / n_0 r_1 (\sim 0.70)$. It is at this H -value where the silica cylinder is acting most strongly as a negative lens; ray refractions or TIRs at the fiber-coating boundary are most strongly counteracting the ray refractions at the coating-air boundary. Also, at this H , the transition from *P* to TIR rays occurs. (ii) The zero value of $d\theta/dH$ at $H \sim 0.62$ implies the formulation of a caustic surface⁸ at the corresponding angle, 18.45 degrees. The bright caustic surface is represented by the peaks in Fig. 2. (iii) At slightly greater scattering angles, light comes from rays originating at $H \sim 0.73$, where $d\theta/dH$ is relatively large, implying a low $P(\theta)$. We therefore predict a high contrast between a bright inner zone (ending at 18.45 degrees) and the angles immediately beyond, just as observed at boundary A. Starting at $H = n_1 r_2 / n_0 r_1 (0.74)$, corresponding to $\theta \approx 38^\circ$, the rays miss the fiber and traverse only the coating. As it should, the plot thereafter coincides with the coating-only case. Also, the sudden decrease in $d\theta/dH$ occurring at 38 degrees predicts boundary B, the start of the outer bright zone.

We see in Fig. 5 how a change in coating refractive index to 1.49

Table I—Conditions for the presence of the various ray types

Types of Rays Present	Conditions on n_0, n_1, n_2, r_1, r_2
	When $E = 0$
<i>P</i>	$n_2 r_2 / n_0 r_1 > 1$
<i>P</i> and TIR	$n_2 r_2 / n_0 r_1 < 1$ and $n_1 r_2 / n_0 r_1 > 1$
<i>P</i> , TIR, and co	$n_1 r_2 / n_0 r_1 < 1$

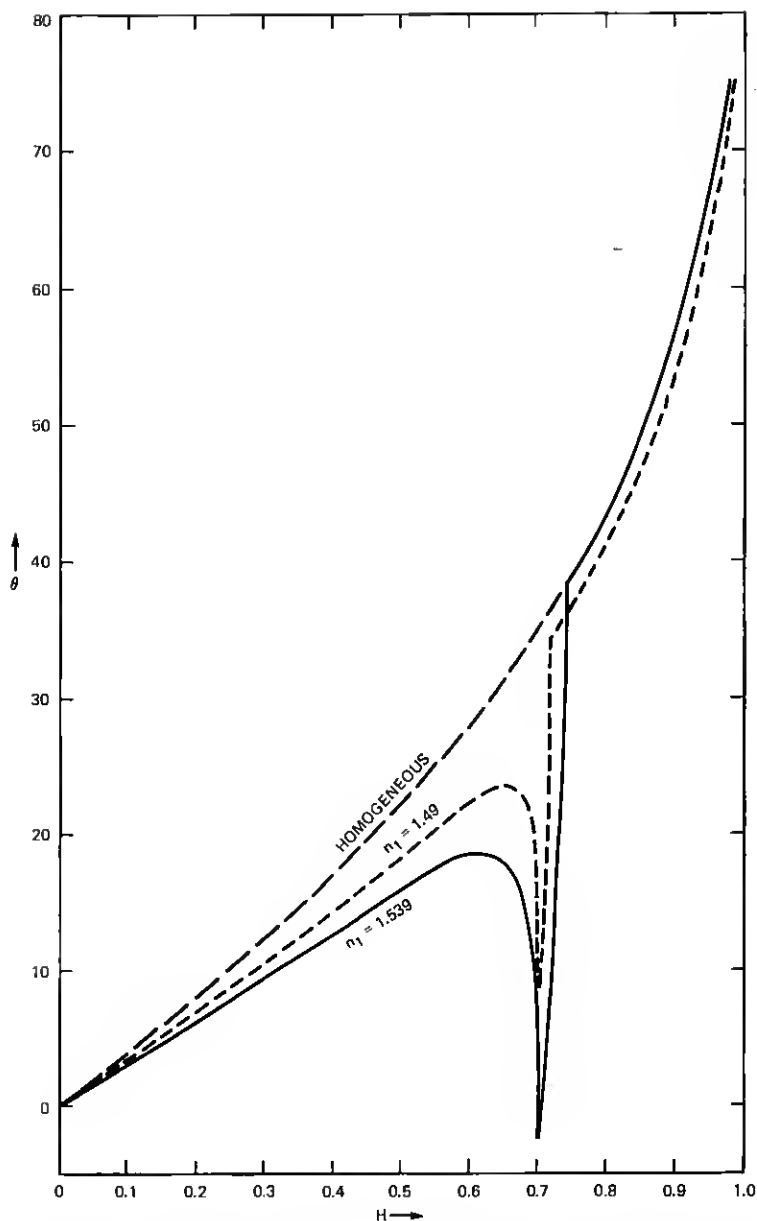


Fig. 5—Plots of θ vs H for three profiles. In all cases, $n_0 = 1.0003$ and $n_2 = 1.457$. For the longer dashes, $r_2/r_1 = 0$ (no fiber, merely a cylinder of coating) and $n_1 = 1.539$. For the solid line, $r_2/r_1 = 0.4812$ and $n_1 = 1.539$. For the shorter dashes, $r_2/r_1 = 0.4812$ and $n_1 = 1.490$.

changes $\theta(H)$ (short dashed lines). The key difference is that the broad peak has narrowed, indicating a decrease in illuminance at the edge of the bright zone. The CO rays do not superimpose on the $n = 1.539$ homogeneous cylinder, since the refractive power is less for the lower index.

Figure 6 indicates how an eccentricity changes the pattern. With dimensions unaltered from Fig. 5, an eccentricity of $10\text{ }\mu\text{m}$ transverse to the incident rays is introduced. We see that the scattering pattern is now asymmetric about $H = 0$ and its orientation relative to the eccentricity is shown in the drawing.

By evaluating a variety of eccentricities, the sensitivity of the scattering pattern to the transverse offset can be ascertained. θ_A and θ_B are plotted against eccentricity in Fig. 7 for left and right sides of the scattering pattern. We see that, for $n_1 = 1.539$ and $r_2/r_1 = 0.4812$, one set of θ_A and θ_B boundaries disappears at $E = \pm 22.4$ and $\pm 26.2\text{ }\mu\text{m}$, respectively, while the other set moves toward the center and remains visible even when the fiber reaches the maximum possible eccentricity. The θ_A disappearance is a result of the previously mentioned TIRs, which can occur as the ray attempts to exit the coating while the θ_B limit, in this case $>90^\circ$, is a manifestation of the maximum refracting

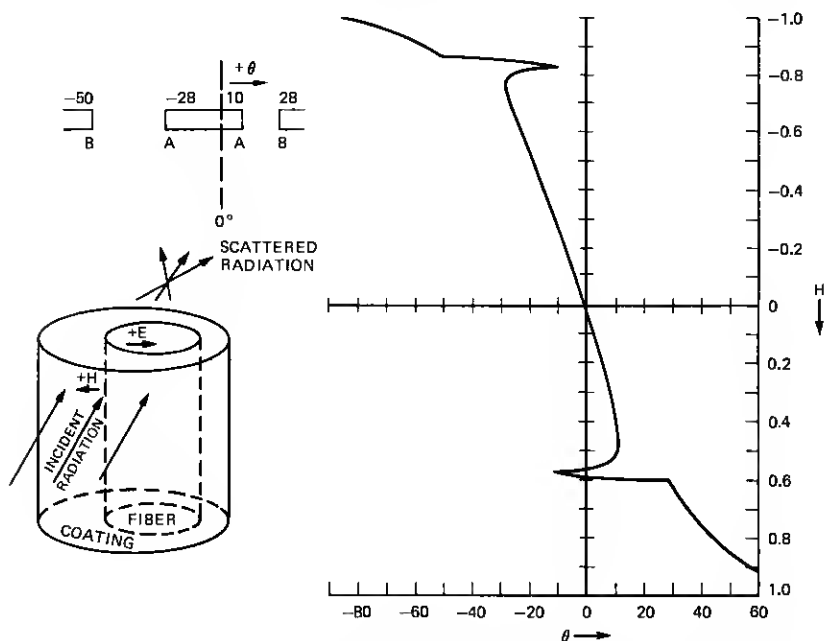


Fig. 6—Plot of θ vs H for the case of Fig. 4. Spatial relationships among E , H , and θ are depicted in the inset. The plotted points are computed.

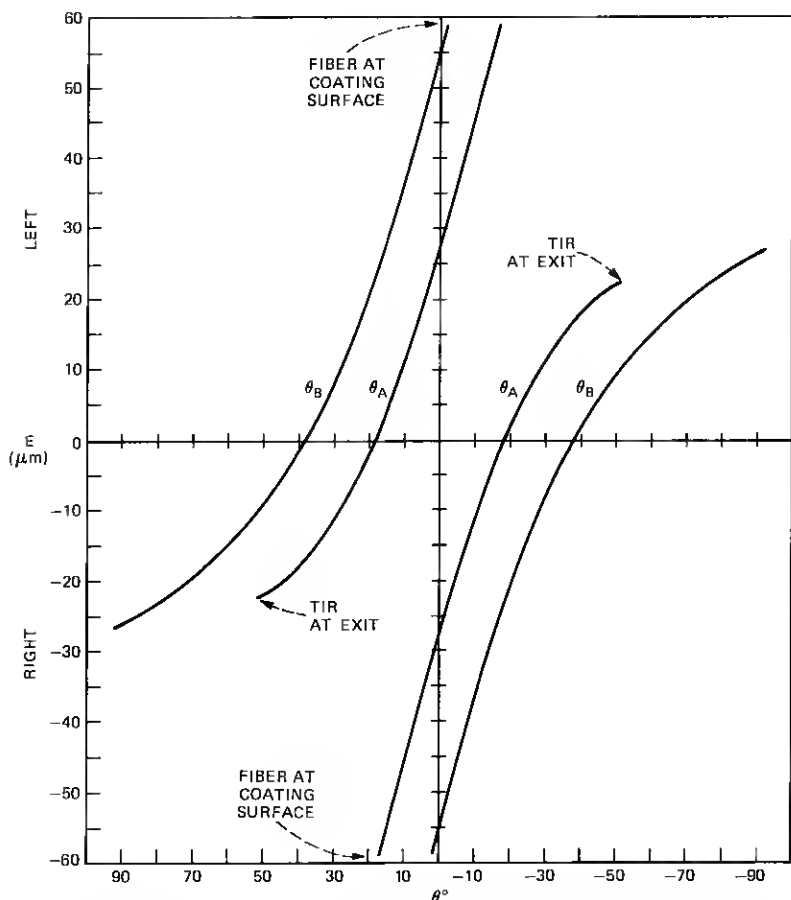


Fig. 7—Plots of θ_A and θ_B on both sides of the scattering pattern as they would appear to an observer as the Fig. 4 fiber coating became eccentric to the left (up) and to the right (down).

power of the coating. Error signals for an automated system are in principle obtainable from the non-disappearing θ_A for all eccentricities. The computed slopes of the Fig. 7 curves at $E = 0$ show a small-eccentricity sensitivity of 0.85 degrees/ μm for the two θ_A 's and 1.1 degrees/ μm for the two θ_B 's.

The angle separating θ_B from θ_A varies with n_1 as other parameters are held constant. Figure 8 illustrates this with plots of θ_A and θ_B as functions of n_1 . θ_A and θ_B also vary significantly with the ratio r_2/r_1 , as shown in Fig. 9. This dependency can conceivably be used for monitoring coating thickness inline, given the fiber diameter. Instrumentation for this would be more complex than that used for merely monitoring eccentricity. Notice that the θ_A caustic disappears when r_2/r_1 is below a certain value (~ 0.10 in Fig. 9). When r_2/r_1 is sufficiently

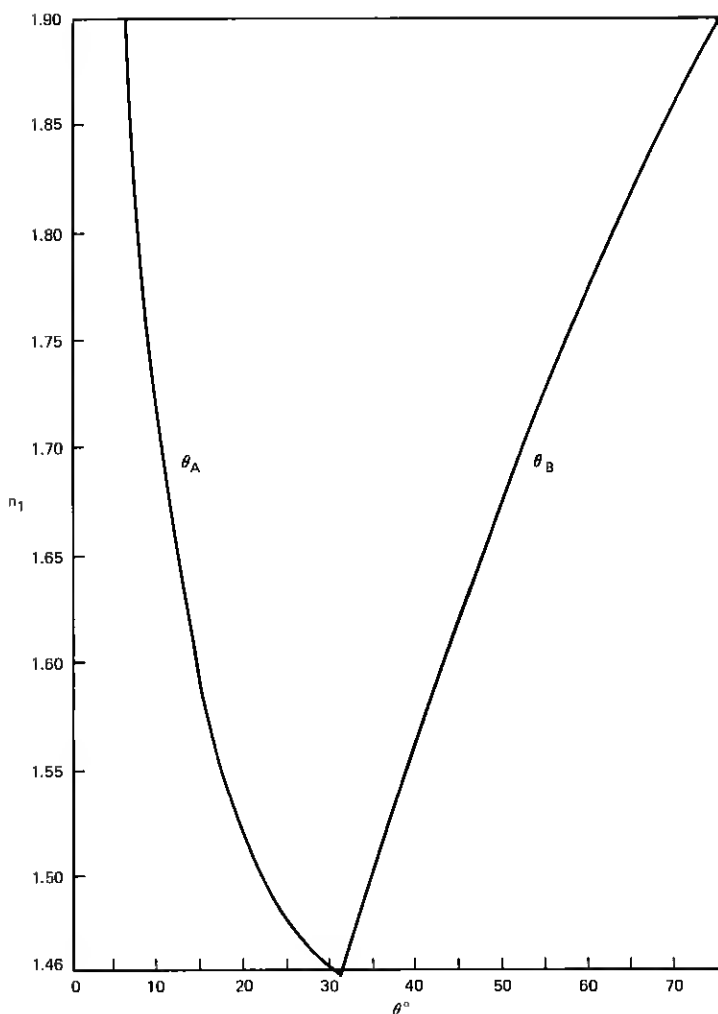


Fig. 8— $\theta_A(n_1)$ and $\theta_B(n_1)$ for the case $n_0 = 1.0003$, $n_2 = 1.4570$, $r_2/r_1 = 0.4812$, and $E = 0$.

small, the negative lensing at the coating-fiber interface is more powerful than the positive lensing of the air-coating interface, even for paraxial rays ($|H| \ll 1$). That is, the condition that the converging wavefront formed by the air-coating interface be refracted to a plane wavefront at the coating-fiber interface leads to the lower θ_A disappearance condition

$$\frac{r_2}{r_1} = \frac{n_0(n_1 - n_2)}{n_2(n_1 - n_0)} \quad (3)$$

derived in Appendix B.

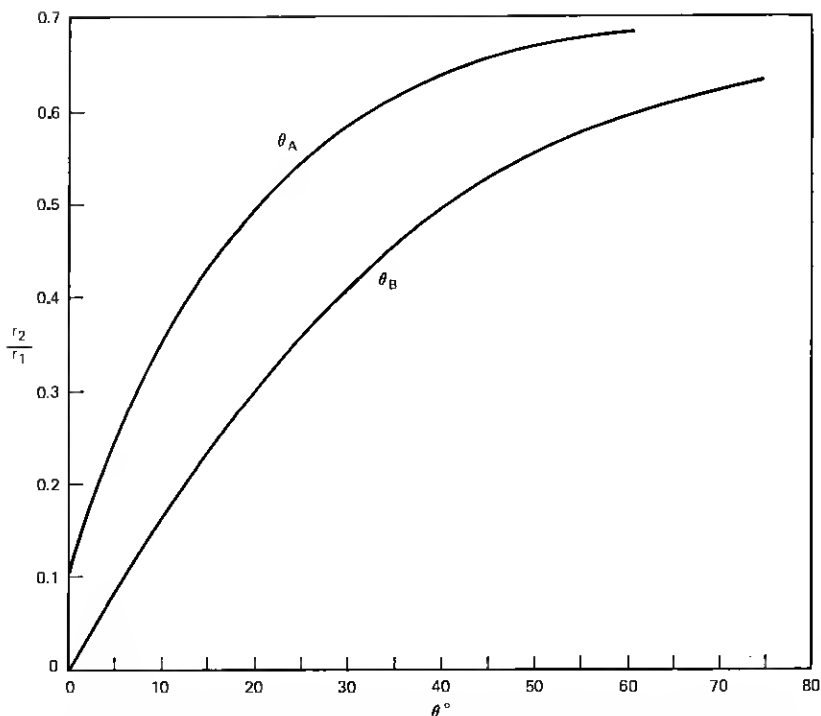


Fig. 9— $\theta_A(r_2/r_1)$ and $\theta_B(r_2/r_1)$ for the case $n_0 = 1.0003$, $n_1 = 1.539$, $n_2 = 1.457$, and $E = 0$. In general, θ_A exists (a caustic forms) when $n_0(n_1 - n_2)/n_2(n_1 - n_0) < r_2/r_1 < n_0/n_2$ and θ_B exists when $r_2/r_1 < n_0/n_1$.

This evaluates to $r_2/r_1 = 0.1045$ for an $n = 1.539$ coating which is the lower θ_A cutoff point, as seen in Fig. 9. In actual fibers, the presence of a higher-index core will tend to slightly decrease the cutoff ratio below that predicted by eq. (3).

IV. COMPARISON WITH EXPERIMENT

The scattering pattern from the well-centered $n = 1.539$ coating shown in Fig. 10 was examined in detail. The fiber was rotated through 360 degrees of azimuth in 10-degree increments, and measurements of the positions of the respective A and B boundaries were made on a screen 47 mm behind the fiber. The wavy nature of the pattern on the screen, seen in Fig. 3, gave each measurement a range of values indicated by the width of the lines in Fig. 11. A statistical summary is given in Table II.

With values of $n_0 = 1.0003$, $n_1 = 1.539$, $n_2 = 1.457$, and $r_2/r_1 = 0.553$, we compared this observed pattern to the theoretically predicted one.

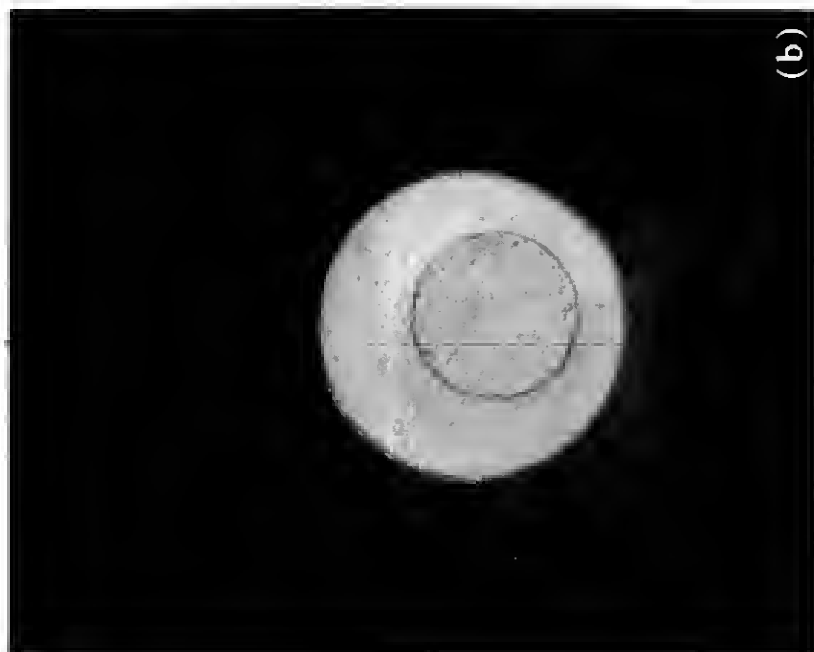
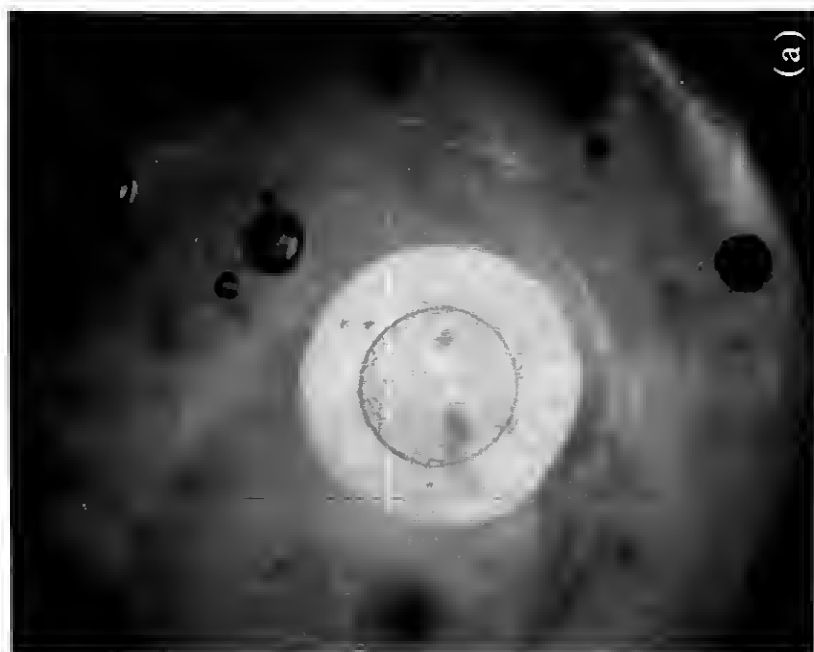


Fig. 10—Cross sections of coated silica (TO-8) fibers when (a) scattering patterns indicated centered geometry and (b) scattering patterns indicated eccentric geometry.

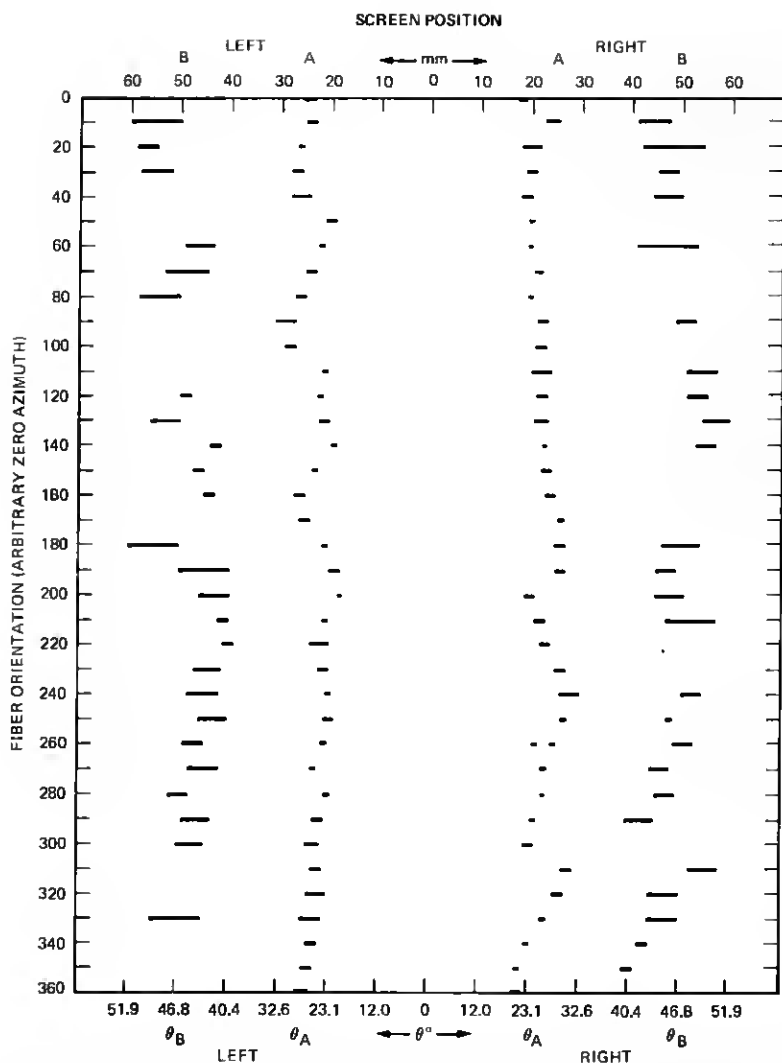


Fig. 11—Values for A and B on both sides of the scattering pattern as the Borden-coated fiber of Fig. 10a was rotated in 10-degree increments. The width of lines represents the position uncertainty due to readability and pattern waviness (see Fig. 3). The screen was 47 mm behind the fiber. Statistics are given in Table 11.

They were mutually consistent: The average measured value of the θ_A was $25.7^\circ \pm 2.7^\circ$ versus $25.4^\circ \pm 1.3^\circ$ predicted from the ray trace. For θ_B , we measured $45.7^\circ \pm 3.2^\circ$ versus $49.4^\circ \pm 2.2^\circ$ predicted. The estimated experimental errors reflect both the distribution in measured values from different azimuths and uncertainty in each single mea-

surement. Theoretical uncertainties arose from inexact knowledge of r_1 and r_2 as obtained from cross sections.

V. USE AS A COATING MONITOR

The pattern's high sensitivity coupled with its easy identifiability fill the requirements of a coating geometry monitor very well. A skewed pattern is interpreted as an error signal. Then, by monitoring scatter patterns from two perpendicular directions, one can guide the coating applicator into proper, centered alignment. Continued monitoring and feedback would compensate for subsequent drifts in the fiber path.

Figure 12 shows a crossed beam setup used to obtain the centered $n = 1.539$ coating over a silica (T08) filament shown in Fig. 10a. Figure

Table II—Comparison of experimental results with theoretical predictions

	A (mm)	θ_A	B (mm)	θ_B
Right side	22.5 ± 2.9	25.6 ± 2.9	48.6 ± 5.2	45.9 ± 3.1
Left side	22.6 ± 2.7	25.7 ± 2.7	47.7 ± 5.6	45.4 ± 3.3
Overall	22.6 ± 2.8	25.7 ± 2.7	48.1 ± 5.4	45.7 ± 3.2
Theoretical		25.4 ± 1.3		49.4 ± 2.2

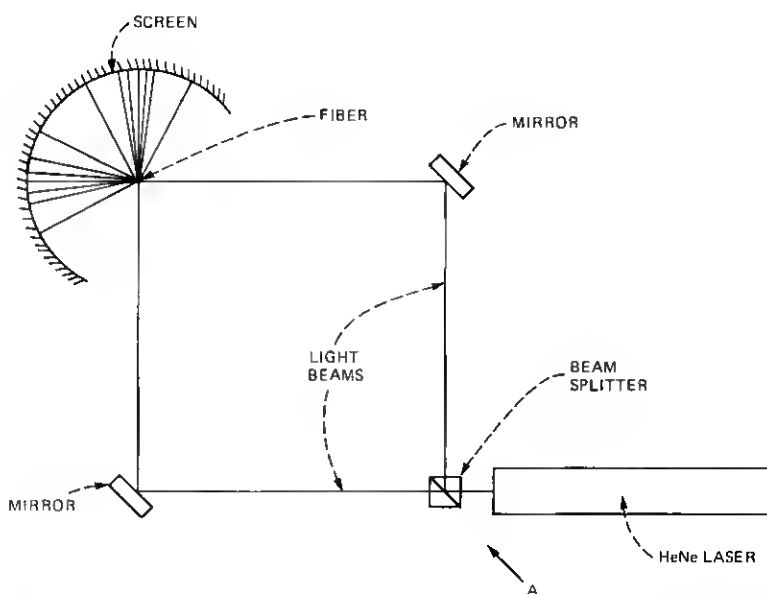


Fig. 12—Plan view schematic of the setup used inline on the Bell Laboratories, Atlanta, drawing machine to monitor coating geometry. The beams are slightly offset vertically to avoid ambiguities on the screen.

10b shows the original eccentric condition before alignment. Vertical beam spread was omitted here and the scattering pattern was a bright modulated horizontal line. An $n = 1.49$ coating was also successfully centered, but the lower refractive index of the coating decreased pattern visibility as compared to the higher-index coating.

A similar crossed-beam monitoring setup was then used on another drawing line to monitor and maintain centering on a 6.6-km length of optical waveguide. Table III shows how eccentricity varied with position as measured on cross sections taken later. Overall, we see excellent centricity, but at the 4.4-km position an unexplainable gross eccentricity occurred. It was traced forward and back and found to have started about 250 m before and ended 100 m after the 4.4-km point. Nothing in the ray trace theory suggests any ambiguity in the pattern at large eccentricities.

In the past, unpublished data had been taken by the author on the results of using alignment techniques which did not utilize light scattering. The best set of data showed a median eccentricity of $12.9 \mu\text{m}$ with other medians from about $15 \mu\text{m}$ to $25 \mu\text{m}$. Also, these other techniques could not detect ongoing changes in alignment during the drawing process.

VI. SUMMARY

We have presented a ray trace model which indicates that the forward scattering pattern from a transversely illuminated optical fiber provides unambiguous data about the eccentricity of the coating under certain conditions of fiber size, coating thickness, and coating refractive index.

Furthermore, the data can be easily interpreted to provide an eccentricity error signal. The ray trace model has been shown to agree well with a closed-form expression of more limited applicability. It also

Table III—Coating geometry of a 6.6-km optical fiber where forward scattering monitoring was used to control coater alignment. Monitoring and feedback started after the 0-km point. The excursion at 4.4 km remains unexplained. Uncertainty of all cross-section measurements is within $\pm 2 \mu\text{m}$.

Distance from Start (km)	Coating Eccentricity (μm)	Glass Diameter (μm)	Coating Diameter (μm)
0.0	46.3	110.6	245.6
1.1	5.0	109.3	252.4
2.2	7.7	108.7	260.7
3.3	2.0	109.8	265.8
4.4	59.5	110.6	256.8
5.5	8.1	110.5	268.2
6.6	9.7	108.7	280.9

matches scattering data from experiments. Finally, when the forward scattering pattern was used to monitor coating geometry inline with the drawing and coating process, the information it provided allowed us to apply well-centered coatings.

VII. ACKNOWLEDGMENTS

It is my pleasure to thank D. L. Myers, R. L. Center (both of Western Electric), and C. R. Lovelace for their help in drawing and coating the fibers, T. A. Lenahan for our discussions of caustic surfaces, M. J. Saunders for his helpful comments on the derivation of eq. (3), and F. R. Wight for his measurements of coating refractive indices.

APPENDIX A

The Concentric Case

An optical fiber and its concentric coating have a refractive index dependent solely on the radial distance from their common center, that is,

$$n = n(r). \quad (4)$$

In such a case, Bouguer's formula¹¹ applies: For a ray lying in a plane perpendicular to the fiber's axis, the product of the local refractive index and the perpendicular distance to the fiber's center is constant along the ray's path, that is,

$$n(r) d(r) = C, \quad (5)$$

where C is the constant and $d(r)$ is the perpendicular distance from the tangent to the ray at r to the center ($r = 0$) (see Fig. 11). From this relationship and symmetry arguments, we derive the dependence of the scattering angle, θ , on the normalized height, H .

First we note, in Fig. 13, the point A where an arbitrary ray BAC , with normalized height H , has traveled half its total distance through a cylinder where $n = n(r)$. We observe a mirror image symmetry for the ray path with respect to the straight line DAF containing the halfway point A and the fiber center F . Since half the refraction occurs on each half of the ray path, then the ray path has turned through an angle $\theta/2$ by the halfway point. Furthermore, this halfway point is the point of minimum r for the ray (assuming some other minimum point leads to either a symmetry violation and/or a contradiction with Bouguer's formula).

In terms of Fig. 13 nomenclature, we have (Ref. 11, p. 123, eq. (10));

$$\int_{\phi_0 + \phi'}^{\phi'} d\phi = \int_{r_1}^{r_{\min}} \frac{Cdr}{R\sqrt{n^2 r^2 - C^2}}. \quad (6)$$

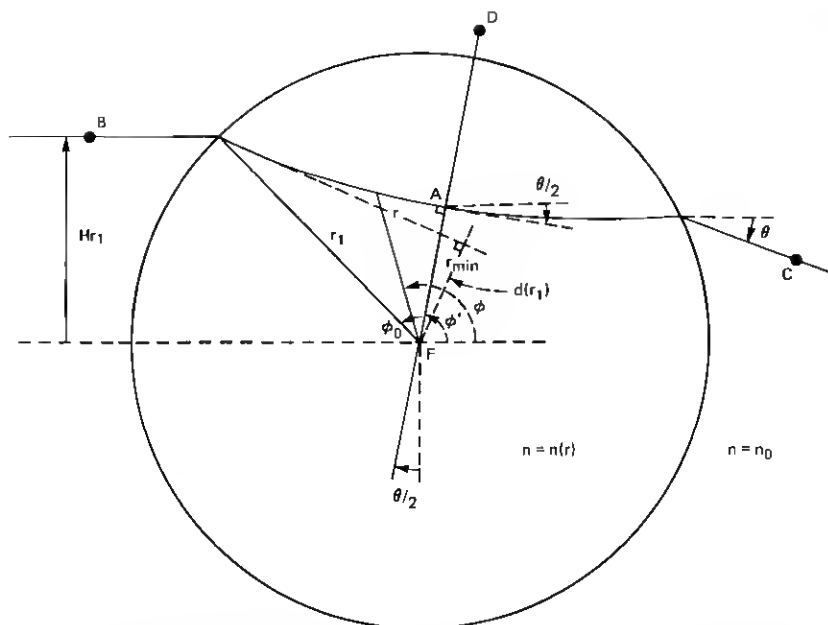


Fig. 13—Nomenclature for derivation of closed form scattering expression from Bouguer's formula (see Appendix A).

Also, from Fig. 11, we have the geometric relations

$$\theta(H) = \pi - 2\phi' \quad (7)$$

and

$$\cos(\phi_0 - \theta/2) = H. \quad (8)$$

For the ray in Figure 11,

$$C = n_0 Hr_1. \quad (9)$$

Substituting eqs. (7), (8), and (9) into eq. (6) and integrating the LHS gives

$$\theta(H) = -2 \cos^{-1}(H) + 2Hr_1n_0 \int_{r_1}^{r_{\min}} \frac{dr}{r\sqrt{n^2r^2 - n_0^2H^2r_1^2}}. \quad (10)$$

For the two cases, (i) ray bypassing the fiber and traversing the coating only and (ii) ray penetrating the fiber, the second term on the right of eq. (10) evaluates to different forms ($n(r)$ makes a step at the coating-fiber interface, $r = r_2$). For a third case, the ray experiences a total internal reflection (TIR) at the coating-fiber interface, $r = r_2$. There,

the turn in the path due to the TIR must be subtracted from $\theta(H)$. After some algebra,¹² the resultant closed forms are

$$\theta(H) = \begin{cases} 2\left(\sin^{-1} H - \sin^{-1} \frac{n_0}{n_1} H\right) & (11a) \\ 2\left(\sin^{-1} H - \sin^{-1} \frac{n_0}{n_1} H + \sin^{-1} \frac{n_0}{n_1} \frac{r_1}{r_2} H\right) - \pi & (11b) \\ 2\left(\sin^{-1} H - \sin^{-1} \frac{n_0}{n_1} H + \sin^{-1} \frac{n_0}{n_1} \frac{r_1}{r_2} H - \sin^{-1} \frac{n_0}{n_2} \frac{r_1}{r_2} H\right), & (11c) \end{cases}$$

where (11a) applies to the coating-only rays ($n_1 r_2 / n_0 r_1 < H < 1$), (11b) applies to the TIR rays ($n_2 r_2 / n_0 r_1 \leq H \leq n_1 r_2 / n_0 r_1$), and (11c) applies to the fiber penetration rays ($0 \leq H < n_2 r_2 / n_0 r_1$).

These expressions were then incorporated into a Fortran program, SCATCF, to determine $\theta(H)$ and $d\theta/dH$ for the concentric coating case.

APPENDIX B

Derivation of Equation (3)

We wish to find a relationship among the radii and refractive indices to generate the behavior of the incident wavefront J as shown in Fig. 14: The incident flat wavefront J is refracted at the cylindrical air-coating boundary of radius r_1 . In the paraxial approximation, the refraction forms a cylindrical wavefront K of radius ρ_1 . It then proceeds a distance $r_1 - r_2$ to L where it has a radius ρ_2 where

$$\rho_2 = \rho_1 - (r_1 - r_2). \quad (12)$$

At this point it undergoes a second refraction at the coating-fiber interface at radius r_2 to again assume the flat shape shown at M . This wavefront behavior, where the paraxial refracting power of the inner cylinder just cancels the outer cylinder's is the limiting case for the disappearance of θ_A (see Fig. 9).

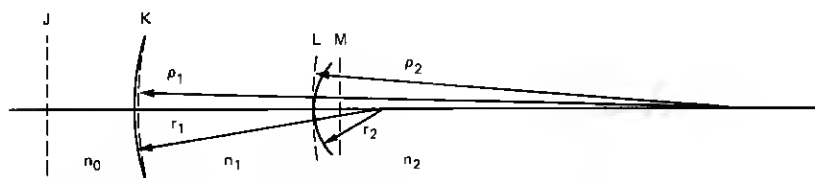


Fig. 14—Nomenclature for derivation of lower cutoff value of r_2/r_1 for existence of θ_A (see Appendix B).

The relationship among n_0 , n_1 , r_1 and ρ_1 is easily derived and given in many texts on geometrical optics. It is a special case of the Gaussian formula for a single spherical surface¹³ (or cylindrical surface for this two-dimensional case). Applied to this case we have

$$\rho_1 = \frac{r_1}{1 - (n_0/n_1)}. \quad (13)$$

The flattening of the wavefront at the second surface is equivalent to a flat front entering from the right and transformed to a front converging to the left with radius ρ_2 . Therefore, again using the Gaussian formula,

$$\rho_2 = \frac{r_2}{1 - (n_2/n_1)}. \quad (14)$$

Combining eqs. (12) to (14) and eliminating ρ_1 and ρ_2 , we arrive at

$$\frac{r_2}{r_1} = \frac{n_0(n_1 - n_2)}{n_2(n_1 - n_0)}, \quad (15)$$

which is eq. (3) in the main text.

REFERENCES

1. A. C. Hart, Jr., and R. V. Albarino, "An Improved Fabrication Technique for Applying Coatings to Optical Fiber Waveguides," Topical Meeting on Optical Fiber Transmission II, February 22-24, 1977.
2. B. Hillerich, P. Rautenberg, D. S. Parmar, and P. Schlang, "Influence of Jacketing on the Transmission Loss of Low-Loss Optical Fibers," Proceedings of 26th International Wire and Cable Symposium, November 15-17, 1977.
3. H. M. Presby, "Geometrical Uniformity of Plastic Coatings on Optical Fibers," B.S.T.J., 55, No. 10 (December 1976), pp. 1525-1537.
4. P. W. France, P. L. Dunn, and M. H. Reeve, "On Line Fiber Coating Using Tapered Nozzles," Third European Conference on Optical Communication, September 14-16, 1977.
5. J. A. Lewis, "Centering Force in the Fiber Coating Applicator," Eighth U.S. National Congress of Applied Mechanics (1978).
6. T. A. Lenahan, "Viscous Centering Force on a Fiber in a Coating Applicator," Summer Meeting for the American Mathematical Society (1978).
7. D. Marcuse and H. M. Presby, "Optical Fiber Coating Concentricity: Measurement and Analysis," Appl. Opt., 16 (1977), p. 2383.
8. M. I. Schwartz and D. Kalish, "Review of Research and Production of High-Strength Fibers," Fifth European Conference on Optical Communication, September 17-19, 1979.
9. B. Hillerich, D. S. Parmar, and P. Schlang, "Criteria for the Jacketing of Optical Fibers," Third European Conference on Optical Communication (1977).
10. L. S. Watkins, "Scattering from Side-Illuminated Clad Glass Fibers for Determination of Fiber Parameters," J. Opt. Soc. Amer., 64 (1974), p. 767.
11. M. Born and E. Wolf, *Principles of Optics*, 2nd ed., New York: Pergamon, 1964, pp. 122-123.
12. I. S. Gradshteyn and I. M. Ryzhik, *Table of Integrals, Series, and Products*, New York: AP, 1965; form 2.271.4 with the substitution $x = 1/r$.
13. Any geometrical optics text, e.g., F. A. Jenkins, and H. E. White, *Fundamentals of Optics*, 3rd ed., New York: McGraw-Hill, 1957, Sections 3.4 and 3.10.